Lateral Currents in Shingle Solar Modules Detected by Magnetic Field Imaging

Nils Klasen ⓘ, Julian Weber ⓘ, Achim Kraft, and Holger Neuhaus

Abstract—**Lateral currents in shingle joints are the driving advantage of shingle matrix modules when it comes to partial shading. In the shingle matrix layout, the shingle joints allow the current to pass shaded regions of the solar module, whereas in other module layouts, the current is blocked by shaded solar cells. We use magnetic field imaging to unveil the current paths in a shingle string and a shingle matrix module under partial shading at 1000 W m^{-2} irradiation with AM1.5 spectrum. The experimental results are compared with a circuit simulation based on an extended two-diode model implemented in *LTspice*.**

Index Terms—**Magnetic field imaging (MFI), matrix interconnection, partial shading, photovoltaic (PV), shingle solar cell interconnection.**

I. INTRODUCTION

PARTIAL shading will become an important aspect to consider when new surfaces in an urban environment are to be utilized to harvest photovoltaic (PV) energy. Building facades and car bodies but also already established rooftop systems are just three examples. Partial shading causes a current mismatch leading to operation points where conductive bypass diodes shortcut parts of the solar modules and decrease the power output drastically.

Work by Schuss et al. [1], [2] and Araki et al. [3] offer detailed insights into dynamic shading and irradiation on vehicles in motion. With this, they define a basis on the irradiation dynamics while driving. Shading losses in roof PV systems in urban areas on the other hand have been discussed extensively by Calcabrini et al. [4] and in a comprehensive review on bypass diodes by Vieira et al. [5]. On system level, Ramaprabha and Mathur [6] investigated the impact of partial shading. These are only a few among many published articles dealing with partial shading of solar cells, modules, and systems. They all commonly state: Because of the electrical series interconnection PV power generators face significant power losses in case of partial shading. Significant losses therefore can be mitigated when solar modules themselves become more shading resilient, i.e., less prone to an internal current mismatch in series interconnected solar cells.

In previous work, we compared the response of various module layouts to partial shading [7], [8] under a representatively large number of shading scenarios using equivalent circuit simulations in *LTspice*. We investigated the conventional 60 solar cell layout, the 120 half-cell "Butterfly"-layout, and two modules with 300 1/5th shingle solar cells, one with a shingle string and one with a shingle matrix layout. We found, that under partial shading, the module with a shingle matrix layout on average produces three times as much power as the conventional layout [8].

One reason for this is an increased number of parallel interconnections in shingle solar cell modules. Parallel interconnections do not suffer from a current mismatch as serial interconnections do and therefore offer advantages with respect to partial shading. However, even for a similar number of parallel interconnected solar cells, we find differences in the partial shading response for a shingle string and a shingle matrix layout [9]. The major reason for this is lateral currents in the shingle joints which in some scenarios, pass shaded areas in the shingle matrix layout instead of being blocked by shaded solar cells in the shingle string layout [9]. So far, these lateral currents have been predicted by our simulations but not proven experimentally.

In this work, we use magnetic field imaging (MFI) for an experimental comparison of shingle string and shingle matrix modules. MFI is a nondestructive imaging method that was introduced to PV community by Lausch et al. in 2018 [10]. As shown in [10], [11], and [12], MFI can be used to detect defects within solar modules such as shunts, broken solder connections, locally poor shingle interconnection, solar cell breakage, etc. Weber et al. [12] further showed that by MFI, the current flow within partially shaded modules can be investigated. In particular, their work contains an exemplary MFI measurement of a small section of a partially shaded shingle matrix module. In our work, we extend their results and correlate simulations with MFI measurements on partially shaded midsized shingle modules including bypass diodes for an exemplary scenario. We experimentally prove the occurrence of the aforementioned lateral currents in partially shaded matrix modules which we consider the striking difference between shingle string and shingle matrix layout for module power output.

This article has been accepted for inclusion in a future issue of this journal. Content is final as presented, with the exception of pagination.

2   IEEE JOURNAL OF PHOTOVOLTAICS
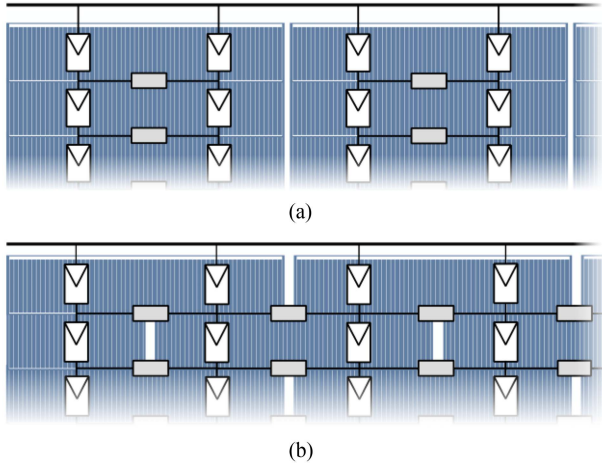
Fig. 1. Principle of solar cell interconnection in (a) shingle string layout and (b) shingle matrix layout. The shingle solar cells are represented by two equivalent circuits, one per half-cell interconnected by a resistor representing the shingle joint and its capability to conduct currents in lateral direction. By using half-cells as base unit, both module layouts are easily implemented by adjusting the network of resistors between the solar cells. Figure is redrawn from [9].

II. MAGNETIC FIELD IMAGING

According to Ampère's law in its differential form, currents in a conductor cause a rotating magnetic field.

$$\text{rot}\left(\vec{B}\right) = \nabla \times \vec{B} = \mu_o \vec{j} + \mu_0 \varepsilon_0 \frac{\partial \vec{E}}{\partial t} \qquad (1)$$

where $\vec{B}$ is the magnetic flux density, $\vec{j}$ the current density in the conductor, $\vec{E}$ the electric field, t the time, μ_0 the vacuum magnetic permeability, and ε_0 the vacuum permittivity. As can be derived from (1), the direction of currents in a solar module can be detected by measuring the magnetic flux density vector. Since the magnitude of $\vec{B}$ decreases quadratic with the radial distance to the conductor [4], it is beneficial in terms of signal strength to bring the magnetic field sensor as close as possible to the conducting structures. A validated method to compute currents directly from the measured magnetic flux density without the knowledge of material permittivities and exact distances to the conductor is not yet available but might be in the future [13]. However, the linear dependency of the magnetic flux density from the current density allows us to compare simulation and experiment qualitatively based on orientation and magnitudes of the signals.

III. METHODOLOGY

A. Solar Module Layouts and Equivalent Circuit Model

As mentioned earlier, we focus on the shingle string and the shingle matrix layout within this work. For both layouts, we experimentally validated our *LTspice*-based model in previous work [9].

In Fig. 1, the shingle string layout is sketched. Solar cells are first interconnected to strings, which are then interconnected in parallel in the final module layout.

TABLE I
SUMMARY OF THE EQUIVALENT CIRCUIT MODEL PARAMETERS FROM [9]

Forward bias	J_{ph} / mA cm^{-2}	39.64 ± 0.0003
	J_{01} / pA cm^{-2}	0.11 ± 0.01
	J_{02} / nA cm^{-2}	23.60 ± 5.45
	R_s / Ω cm^2	0.57 ± 0.07
	R_p / kΩ cm^2	130.53 ± 128.07
Reverse bias	J_{Br} / mA cm^{-2}	562.97 ± 143.58
	V_{Br} / V	-29.74 ± 1.52
	n_{Br} / 1	27.84 ± 5.21

TABLE II
CHARACTERISTIC VALUES OF THE MODULES AT STC MEASURED AT CALLAB PV MODULES AT FRAUNHOFER ISE

	Shingle string layout	Shingle matrix layout
I_{SC} / A	7.17 ± 0.11	7.23 ± 0.11
V_{OC} / V	12.13 ± 0.08	12.16 ± 0.08
FF / %	77.50 ± 1.09	75.22 ± 1.06
I_{MPP} / A	6.75 ± 0.13	6.69 ± 0.13
V_{MPP} / V	9.99 ± 0.10	9.89 ± 0.10
P_{MPP} / W	67.46 ± 1.22	66.11 ± 1.20

The string length is defined by bypass diodes along the serial interconnected solar cells. Fig. 1(b) shows the shingle matrix layout. In this layout, solar cells are shifted by a half-cell in lateral direction with respect to each other to form a brick wall-like network, or matrix, of solar cells. In the shingle matrix layout, the solar cells are interconnected in parallel in each row followed by a serial interconnection of the rows in the final layout. Again, bypass diodes are used to define sections in the module.

We define the half-cut shingle solar cells as the base unit and represent them with an extended two-diode equivalent circuit model. By this, both layouts can be generated by arranging ohmic resistors representing the conductivity of the shingle joints in lateral direction. The so-created network is then input into *LTspice* which solves the resulting system of equations to compute the I-V-characteristic of the solar module. As input, we use I-V-characteristics of 30 PERC solar cells including their reverse breakdown. The average model parameters and their statistical standard deviation are given in Table I. The diode ideality factors are set to $n_1 = 1$ and $n_2 = 2$. Out of this set of solar cell characteristics, we randomly assign the obtained two-diode parameters to the base unit equivalent circuits. More details on the model can be found in [9].

The modules used in this work for experiment and simulation are shown in Fig. 2. They each consist of 72 monofacial shingle solar cells, organized in an array of 18×8 base units (half-shingle solar cell). Both modules approximately feature identical short-circuit current I_{SC} and open-circuit voltage V_{OC}. Their characteristic values measured under STC are given in Table II.

A module connector in the center allows the implementation of two bypass diodes defining an upper and a lower block within the solar modules. Thus, both modules include all parts of a commercial solar module and can therefore be considered representative for full-size shingle modules. We used an ethylene-vinyl acetate copolymer as encapsulant, $3.2-$ mm thick solar float glass as front cover and a transparent PET backsheet.

This article has been accepted for inclusion in a future issue of this journal. Content is final as presented, with the exception of pagination.

KLASEN et al.: LATERAL CURRENTS IN SHINGLE SOLAR MODULES DETECTED BY MAGNETIC FIELD IMAGING 3
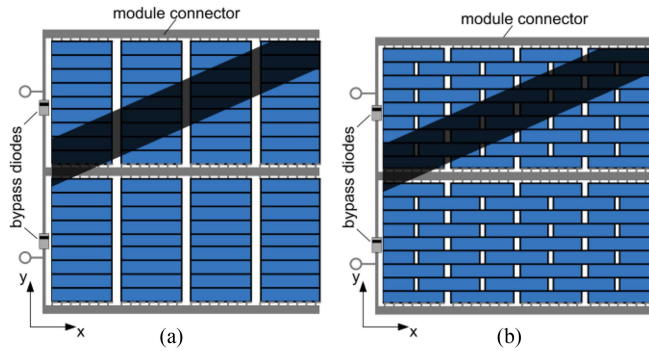

Fig. 2. Schematic drawing of (a) shingle string and (b) shingle matrix module used in the shading experiments. Both modules consist of 72 shingle solar cells each, arranged to an array of 18×8 base units (half-shingle solar cell). Two bypass diodes and a module connector in the center define an upper and a lower block. The investigated shading scenario is a diagonal shade that primarily covers the upper block.

During the experiments, an opaque cartridge of $100\,\mathrm{mm}$ width is used to simulate a diagonal shade in the upper block. This is also sketched in Fig. 2. Note that where the cartridge is applied, the solar cells are not entirely shaded but receive a small remaining fraction of the illumination. One of the reasons for that is that the cartridge itself is not fully opaque. In the chosen shading scenario, one solar cell per string is entirely covered, such that the corresponding photocurrent is close to zero. In the shingle string layout, this should lead to a current reduction in the upper block also close to zero, while in the shingle matrix layout, we expect the current to be reduced only by the fraction of shaded area per row. The latter requires lateral currents along the shingle joints to bypass the shaded area, as we already discussed in [9].

B. MFI Measurements During Partial Shading

For the two shingle modules and the shading scenario sketched in Fig. 2, MFI measurements are carried out in an *Eternalsun spire BBA* solar simulator at $1000\,\mathrm{W\,m^{-2}}$ irradiation and AM1.5 spectrum. The MFI setup is sketched in Fig. 3. Under these conditions, the steady-state module temperature is around $50\,°\mathrm{C}$. Before the experiments, the modules are kept inside the solar simulator for $2\,\mathrm{h}$. A pt100 sensor in the center of the modules ensures that steady-state conditions are reached. Before the MFI measurements, this sensor is removed as it would disturb the measurement itself. The I-V-characteristics are measured with a *Halm cetis PV-CT-F1* setup. Because of the negative temperature coefficient for the open-circuit voltage caused by a decreasing bandgap at elevated temperatures, the module voltage is reduced in the experiments in comparison to the simulations.

Furthermore, the ohmic losses are increased because of cabling and the increased operating temperature. Thus, the fill factor is smaller in experiment than in simulation.

The solar modules stand upright and are illuminated from the front. The MFI characterization is carried out from the rear with a sensor array containing 64 individual sensors. The minimum resolution of $\vec{B}$ is $1\,\mu\mathrm{T}$. The sensor array is scanned across the rear side of the module by a x-y-stage with a working distance of $< 2\,\mathrm{mm}$.
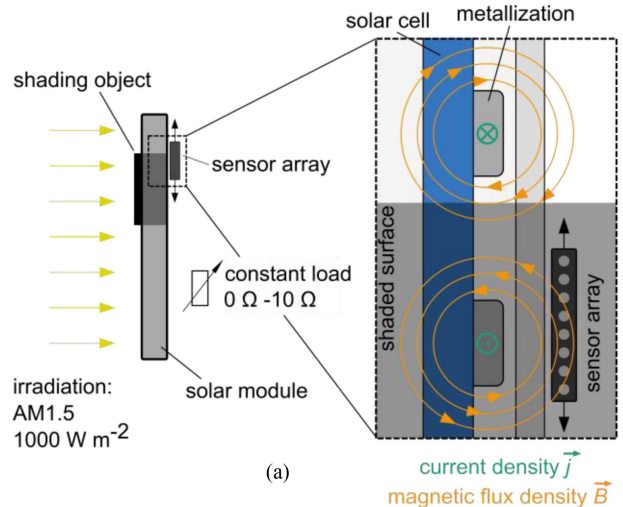

Fig. 3. (a) Sketched setup in our shading experiment to measure the magnetic flux density $\vec{B}$ by MFI. The close-up view is meant to illustrate the principal correlation between the current density in the solar module and the resulting magnetic flux density and is not to scale. The solar module is illuminated from the front while the MFI is done from the rear. During the experiments, the operation point of the solar module is adjusted by a constant load between $0\,\Omega$ and $10\,\Omega$. (b) Image of the setup in the solar simulator. The area covered with solar cells (highlighted green) is $630\,\mathrm{mm} \times 560\,\mathrm{mm}$. The sensor array (highlighted red) is visible through the transparent back sheet.

During the experiments, the operation points of the solar modules are kept constant by an external load that can be adjusted to a resistance between $0\,\Omega$ and $10\,\Omega$. Using a multimeter, the module voltage is monitored while adjusting the constant load until the MPP voltage is reached. Before the characterization, a background measurement is conducted in open-circuit conditions. The background is then subtracted from the data during postprocessing.

IV. RESULTS AND DISCUSSION

A. Shingle String Module

Fig. 4(a) again shows the chosen shading scenario for reasons of comparison and discussion of subfigures (c)–(f). The measured and computed I-V-characteristics for this scenario

This article has been accepted for inclusion in a future issue of this journal. Content is final as presented, with the exception of pagination.
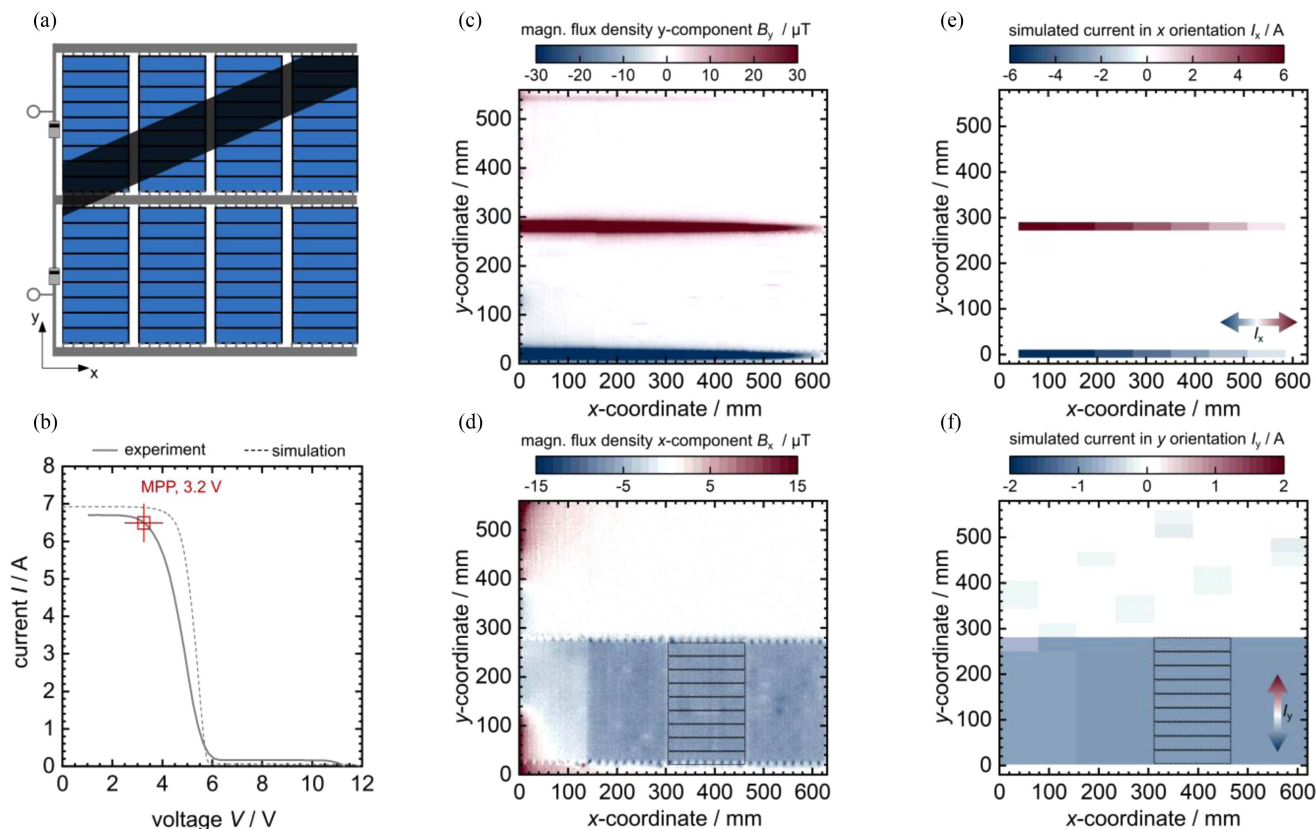
4   IEEE JOURNAL OF PHOTOVOLTAICS

Fig. 4. (a) Shading of the shingle string module during the experiment and (b) I-V-characteristic measured and simulated for this specific shading scenario. The components (c) B_y and (d) B_x obtained by MFI for the maximum power point (MPP) at 3.2 V correlate with the computed currents (e) I_x and (f) I_y. In (d) and (f), the individual solar cells of one string of the lower block are sketched. Note that the simulation is based on a lumped parameter model with half-cut shingle solar cells as smallest unit while the MFI data are spatially resolved.

are shown in Fig. 4(b). As intended in experiment, the upper block does not generate significant currents. Consequently, the current is close to zero for voltages V > 6 V. As discussed in Section III, a small fraction of current remains. In maximum power point (MPP) operation, the bypass diode of the upper block is conductive. This is the operation point during the MFI measurement realized by adjusting the load resistor accordingly.

In the simulations shown in Fig. 4(e), the module current enters the solar module via the center connector orientated in x-direction, where it gradually distributes on the strings of the lower block. We find an opposed current flow in the lower module connector and a good correlation to the B_y component in the MFI measurement [Fig. 4(c)]. Even though the major fraction of current enters the module via the center connector, we find a small B_y-signal on the upper connector caused by the remaining current generated in the upper block.

Concerning the photocurrents in the upper block orientated in y-direction [see Fig. 4(d)], we find them to be close to zero. Also in this sense, we find good agreement with the simulation results [see Fig. 4(f)], within the method's scaling constraints as described in Section II.

In the lower block, the first solar cell in the string on the very left is slightly affected by the shade and therefore the overall current of the string is reduced compared with the other strings of the lower block.

A strong positive B_x signal close to the left edge is caused by the high current densities in the module connectors towards the junction box adjacent to the solar cells and can be treated as a measurement artifact. Overall, we find the simulation and measurement to be in excellent agreement in major as well as minor aspects of the current flow in the solar module during partial shading.

B. Shingle Matrix Module

For the identical shading scenario, we find a different outcome for the shingle matrix layout [Fig. 5(a)]. Since the solar cells in each row act like one large solar cell, the current is only reduced by the shaded area fraction in the row of maximum shading [9]. This requires lateral currents to flow in x-direction through the network of shingle joints and therefore become visible in MFI as B_y component. For the chosen shading scenario, the current generated by the upper block is roughly reduced by one-third compared with full illumination [Fig. 5(b)]. That results in an MPP voltage close to the unshaded case without any bypass diode in conductive state. Hence, both blocks contribute to the MPP voltage and since they are in a serial interconnection, they both generate the same current. Fig. 5(c) and (e) show in good agreement that the current enters the solar module via the upper module connector and leaves it via the lower module connector.
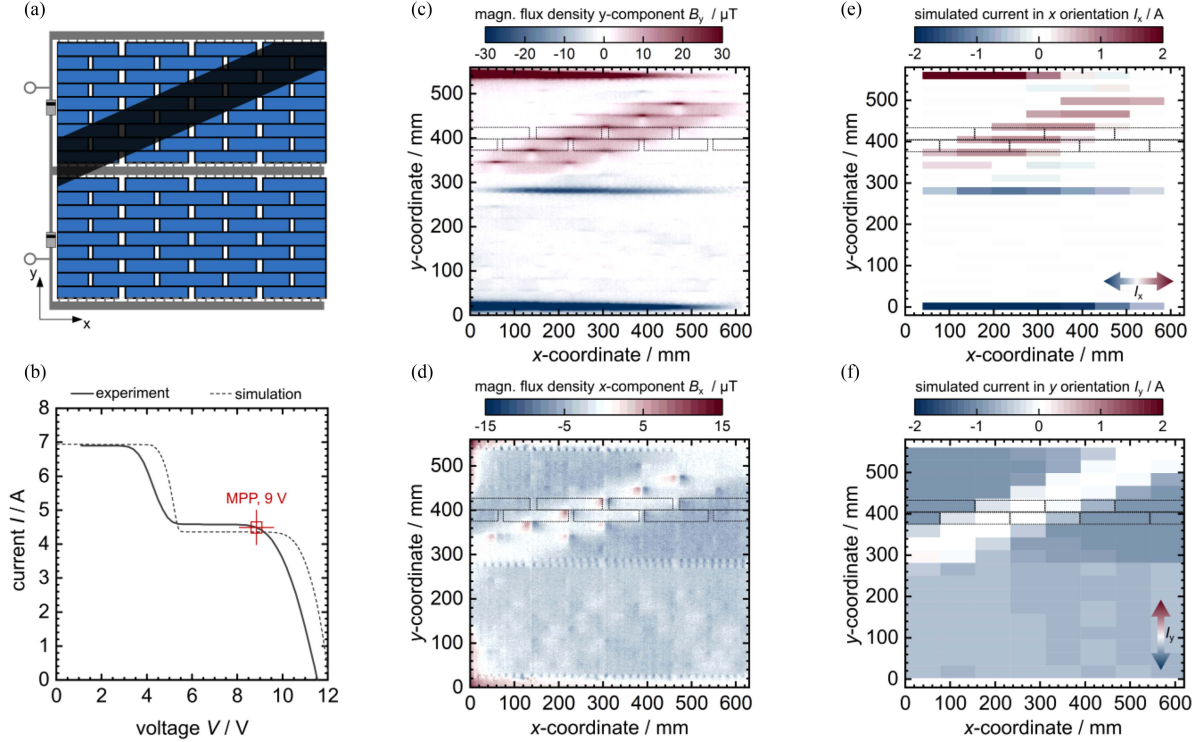
This article has been accepted for inclusion in a future issue of this journal. Content is final as presented, with the exception of pagination.

KLASEN et al.: LATERAL CURRENTS IN SHINGLE SOLAR MODULES DETECTED BY MAGNETIC FIELD IMAGING   5

Fig. 5. (a) Shading of the shingle matrix module during the experiment and (b) I-V-characteristic measured and simulated for this specific shading scenario. The components (c) B_y and (d) B_x obtained by MFI for the maximum power point (MPP) at 9.0 V correlate with the computed currents (e) I_x and (f) I_y. In (c) to (f), two rows of solar cells of the upper block are sketched. Note that the simulation is based on a lumped parameter model with half-cut shingle solar cells as smallest unit while the MFI data are spatially resolved.

The major difference between the shingle string and shingle matrix layout becomes evident, when looking at the B_y signal within the upper block. Where the shade covers the surface of the solar module, we find a B_y signal corresponding to currents in positive x-direction. In this main aspect responsible for the increased shading resilience of the shingle matrix layout, we find a very good agreement between the simulation and the experiment.

Two rows of solar cells have been sketched in Fig. 5(c) and (e) to show that the highest current densities are located at the transition of two adjacent solar cells within one row. There, the current path over a short distance is limited to only one silver busbar. We also find that the lateral current flow is not limited to the shingle joint but is also present in the aluminum rear electrode of the monofacial solar cells. In the shaded area, the MFI image in Fig. 5(d) even resolves $\vec{B}$ components in the rear electrode close to the solar cell edges showing current flows towards the transition just before and after the transition pointing away from it towards the solar cell center.

Since the currents in the upper block pass the shade from left to right, the overall generated current accumulates on the right side of the upper block. Fig. 5(c) and (e) indicate that, in the following, the current flows in the center interconnector from right to left and thereby redistributes homogeneously on the lower block. This explains, why an increasing signal is measured with a maximum around $x = 200\,\mathrm{mm}$ to $x = 300\,\mathrm{mm}$ followed by a decreasing signal towards $x = 0\,\mathrm{mm}$.

We find a decent B_x signal in Fig. 5(d) on a major fraction of the solar module surface representing the generated photocurrents. In the shaded areas, the B_x signal is close to zero except for the before-mentioned currents towards the transitions between two adjacent solar cells in one row.

The magnitude of the B_x signal within the illuminated area of the upper block is slightly larger than in the lower block. This is because of the current match of both blocks at 9.0 V and the fact, that this current in the lower block is generated on a larger surface, which in consequence lowers the current density and thus the B_x component. Again, MFI proves its capability to detect and visualize details of the current flow within the investigated solar modules as they are computed by the *LTspice* model.

C. Line Scan Comparison

A semiquantitative conclusion is drawn from two line scans, one per module. To have a strong MFI signal and since the equivalent circuit model offers no spatial resolution, we chose the center module connector for this evaluation. Along the line scans, we normalize the data with the maximum observed amplitude $|B_{y,\mathrm{max}}|$ and $|I_{x,\mathrm{max}}|$ for measurement and simulation respective. The result is shown in Fig. 6.

We want to emphasize that by comparing both normalized data sets we cannot claim quantitative accordance between measurement and simulation. Still, this evaluation reinforces the
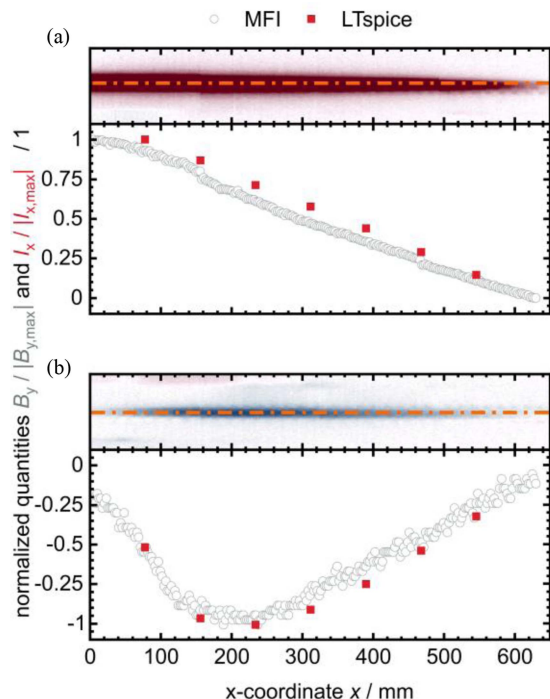
Fig. 6.   Line scan comparison between measured magnetic flux densities B_y and computed currents I_x in the center module connector for (a) shingle string module and (b) shingle matrix module. To compare experiment to simulation the data are normalized with the maximum amplitudes $|B_{y,max}|$ and $|I_{x,max}|$ along the line scan.

agreement derived from Figs. 4 and 5 by showing that along the evaluation line the same trends in the data are eminent.

In case of the shingle string module in Fig. 6(a) we find the current to linearly decrease from $x = 0$ mm to $x = 630$ mm. Along with the current we also find a mostly linear decrease in the magnetic flux density although it especially in the module center is below the computed values. A reason for this is the larger gap between sensor and conductor, which is largest in the module center.

In case of the shingle matrix module in Fig. 6(b), we find a maximum amplitude for both B_y and I_x around $x = 200$ mm. Note that the negative values result from the orientation of the current which in this case is from right to left resulting. After the currents passed the shaded areas from left to right in the upper block, they redistribute in the center connector. Hence, the current increases from $x = 630$ mm towards $x \cong 200$ mm followed by a decreasing current from $x = 200$ mm to $x = 0$ mm. The slightly smaller amplitude in the MFI data might originate from the normalization with $|B_{y,max}|$ instead of using an average value around $x = 200$ mm. Besides this location of the maximum amplitude as well as the slopes in both measured magnetic flux density and computed current show a good correspondence.

V. CONCLUSION

We find an excellent agreement down to details between simulations and experimental characterization with regards to the current flow in shingle solar modules subjected to partial shading. So far, only predicted by simulations, MFI makes lateral currents in shingle matrix modules visible for the first time in experiments. This property of the shingle matrix layout is the major reason for its exceptional partial shading behavior as shown in previous simulation studies [8]. This work also underlines MFI as a nondestructive characterization method not only in fault-detection but also for the investigation of module shading.

REFERENCES

[1] C. Schuss, T. Kotikumpu, B. Eichberger, and T. Rahkonen, "Impact of dynamic environmental conditions on the output behaviour of photovoltaics," in *Proc. 20th IMEKO TC4 Int. Symp. 18th Int. Workshop ADC Model. Testing Res. Electric Electron. Meas. Econ. Upturn*, 2014, pp. 993–998. [Online]. Available: https://www.imeko.org/publications/tc4-2014/IMEKO-TC4-2014-437.pdf

[2] C. Schuss, B. Eichberger, and T. Rahkonen, "Impact of solar radiation on the output power of moving photovoltaic (PV) installations," in *Proc. IEEE Int. Instrum. Meas. Technol. Conf.*, 2018, pp. 1–6.

[3] K. Araki et al., "Rough and straightforward estimation of the mismatching loss by partial shading of the PV modules installed on an urban area or car-roof," in *Proc. 46th Photovolt. Specialists Conf.*, 2019, pp. 1218–1225.

[4] A. Calcabrini, R. Weegink, P. Manganiello, M. Zeman, and O. Isabella, "Simulation study of the electrical yield of various PV module topologies in partially shaded urban scenarios," *Prog. Sol. Energy*, vol. 225, pp. 726–733, 2021, doi: 10.1016/j.solener.2021.07.061.

[5] R. G. Vieira, F. M. U. de Araújo, M. Dhimish, and M. I. S. Guerra, "A comprehensive review on bypass diode application on photovoltaic modules," *Energies*, vol. 13, no. 10, 2020, Art. no. 2472, doi: 10.3390/en13102472.

[6] R. Ramaprabha and B. L. Mathur, "A comprehensive review and analysis of solar photovoltaic array configurations under partial shaded conditions," *Int. J. Photoenergy*, vol. 2012, pp. 1–16, 2012, doi: 10.1155/2012/120214.

[7] N. Klasen, F. Lux, D. Weißer, T. Roessler, and A. Kraft, "Analysis of the impact of partial shading on various module topologies," in *Proc. 38th Eur. Photovol. Sol. Energy Conf. Exhib.*, 2021, Art. no. 181375.

[8] N. Klasen, F. Lux, J. Weber, T. Roessler, and A. Kraft, "A comprehensive study of module layouts for silicon solar cells under partial shading," *IEEE J. Photovolt.*, vol. 12, no. 2, pp. 546–556, Mar. 2022, doi: 10.1109/JPHOTOV.2022.3144635.

[9] N. Klasen, D. Weißer, T. Geipel, D. H. Neuhaus, and A. Kraft, "Performance of shingled solar modules under partial shading," *Prog. Photovolt.: Res. Appl.*, vol. 30, no. 4, pp. 325–338, 2021, doi: 10.1002/PIP.3486.

[10] D. Lausch et al., "Magnetic field imaging (MFI) of solar modules," in *Proc. 35th Eur. Photovolt. Sol. Energy Conf. Exhib.*, 2018, Art. no. 020021, doi: 10.4229/35thEUPVSEC20182018-5BO.11.5.

[11] A. Paduthol et al., "Magnetic field imaging: Strengths and limitations in characterising solar cells," in *Proc. 46th Photovolt. Specialists Conf.*, 2019, pp. 822–824.

[12] J. Weber, S. Hoffmann, K. Kaufmann, and A. De Rose, "Magnetic field imaging (MFI) of shingle solar modules," in *Proc. IEEE 49th Photovolt. Specialists Conf.*, 2022, pp. 0231–0231.

[13] O. Kunz et al., "Investigating metal-semiconductor contacts in solar cells using magnetic field measurements," in *Proc. 46th Photovolt. Specialists Conf.*, 2019, pp. 2764–2768.